

## High-Energy Emission from a Solar Flare in Hard X-rays and Microwaves

M.R. Kundu<sup>1</sup> · V.V. Grechnev<sup>2</sup> ·  
S.M. White<sup>1</sup> · E.J. Schmahl<sup>1,3</sup> ·  
N.S. Meshalkina<sup>2</sup> · L.K. Kashapova<sup>2</sup>

© Springer ●●●

### Abstract

We investigate accelerated electron energy spectra for different sources in a large flare using simultaneous observations obtained with two instruments, the Nobeyama Radio Heliograph (NoRH) at 17 and 34 GHz, and the Reuven Ramaty High Energy Solar Spectroscopic Imager (RHESSI) at hard X-rays. This flare is one of the few in which emission up to energies exceeding 200 keV can be imaged in hard X-rays. Furthermore, we can investigate the spectra of individual sources up to this energy. We discuss and compare the HXR and microwave spectra and morphology. Although the event overall appears to correspond to the standard scenario with magnetic reconnection under an eruptive filament, several of its features do not seem to be consistent with popular flare models. In particular we find that (1) microwave emissions might be optically thick at high frequencies despite a low peak frequency in the total flux radio spectrum, presumably due to the inhomogeneity of the emitting source; (2) magnetic fields in high-frequency radio sources might be stronger than sometimes assumed; (3) sources spread over a very large volume can show matching evolution in their hard X-ray spectra that may provide a challenge to acceleration models. Our results emphasize the importance of studies of sunspot-associated flares and total flux measurements of radio bursts in the millimeter range.

**Keywords:** Flares, Impulsive Phase; X-Ray Bursts, Hard; Radio Bursts, Microwave (mm, cm)

---

<sup>1</sup>Astronomy Department, University of Maryland, College Park, MD 20742 email: kundu@astro.umd.edu email: ed@astro.umd.edu email: white@astro.umd.edu

<sup>2</sup>Institute of Solar-Terrestrial Physics, Irkutsk 664033, Russia email: grechnev@iszf.irk.ru

<sup>3</sup>Lab for Astronomy and Solar Physics, NASA Goddard Space Flight Center, Greenbelt, MD 20771

## 1. Introduction

Energetic electrons accelerated to energies of tens and hundreds of keV can be observed through microwave and hard X-ray (HXR) emissions from the solar corona. Imaging observations are important to study the origin of energetic electrons in large flare events, which in turn can be used to test flare models and other related theoretical issues. Two dedicated solar imaging instruments most important for studies of solar flares are at present available — one in X-rays and gamma-rays by the Reuven Ramaty High Energy Solar Spectroscopic Imager (RHESSI, Lin *et al.*, 2002) and the other in microwaves by the Nobeyama Radioheliograph (NoRH, Nakajima *et al.*, 1994) at 17 and 34 GHz. NoRH is capable of imaging signatures of microwave emitting electrons in flaring sources. At 17 GHz it measures both Stokes  $I$  and  $V$ , and at 34 GHz Stokes  $I$  alone, with good sensitivity and spatial resolution of  $\approx 10''$  and  $\approx 5''$ , respectively at the two frequencies. Signatures of hard X-ray emitting electrons are mapped by RHESSI. RHESSI's primary objective is the study of energy release and particle acceleration in solar flares. This is accomplished by imaging spectroscopy of solar hard X-rays and gamma-rays over a 3 keV to 17 MeV energy range with energy resolution of  $\approx 1$  keV, time resolution of  $\approx 4$  s or better and spatial resolution as high as  $2.3''$ .

Non-thermal microwave emission during large solar flares is produced by the gyrosynchrotron mechanism which involves coronal magnetic fields of at least a few hundred gauss and electrons of hundreds of keV and higher energy. Hard X-ray emission, on the other hand, is mainly produced by bremsstrahlung from precipitating electrons of tens to hundreds of keV energies. The two different methods of mapping energetic flare electrons therefore complement each other, and provide good means of testing flare-related concepts which have been abundant in the recent literature. The major hard X-ray flux is emitted by precipitating electrons striking a thick target, whereas microwaves are emitted by electrons gyrating in magnetic fields, both precipitating and trapped in coronal magnetic tubes.

Several issues related to accelerated electrons in solar flares are debated in the literature. First, it is not clear if a single acceleration mechanism operates in a flare or different mechanisms contribute (*e.g.*, Wild, Smerd, and Weiss, 1963; Bogachev and Somov, 2001). Note that the possible presence of different “accelerators” does not necessarily show up in the shape of the electron spectrum (Bogachev and Somov, 2007). One cannot also rule out the possibility that in an event with repetitive acceleration/injection episodes part of an electron population accelerated in the previous episode undergoes an additional acceleration from basically the same mechanism.

One more question is related to the fact that the electron spectra inferred from microwave observations at frequencies believed to be optically thin appear to be harder than those inferred from HXR data as initially shown by Kundu *et al.* (1994) and repeatedly confirmed afterwards. Following the interpretation of Melnikov and Magun (1999), other researchers (*e.g.*, Silva, Wang, and Gary, 2000; Lee, Gary, and Shibasaki, 2000; Takasaki *et al.*, 2007) suggest that this fact

can be explained by the collisional hardening of the electron spectra in magnetic traps.

Another possibility was proposed by White *et al.* (2003) who considered high-frequency radio emissions at 35 and 80 GHz in the well-studied flare of 23 July 2002. From the analysis of the microwave/millimeter and HXR data they concluded that the trapping could not explain the difference between the electron indices inferred from these emissions in that event. They were “forced to assume that ... the 35–80 GHz spectrum does not represent optically thin emission” due to contamination at high frequencies by a component with a very high turnover frequency. This event required a very large number of emitting electrons with a hard spectrum, which they indeed found in that event, up to  $10^{10} \text{ cm}^{-3}$  above 20 keV with a power-law index  $\delta \approx 4.5 - 5$ . The conclusion of White *et al.* (2003) suggests that a similar situation might occur in other events; with a lesser number of power-law electrons, the optically thick regime could reach high radio frequencies if magnetic fields are strong.

Here we discuss the RHESSI HXR and NoRH microwave imaging observations of the flare of 17 June 2003. The flare in question was of class M6.8, and it was observed in AR 10386 (S08 E58), a  $\beta\gamma\delta$ -region, two days after its east-limb passage. This flare produced a multitude of strong, isolated bursts seen in HXR and microwaves, combining a few similar events occurring at nearly the same place under similar conditions and promising important information on accelerated electrons. This flare was previously discussed by Ji, Huang, and Wang (2007) in the context of motions of flare loops. In our paper, we address high-energy emissions observed during this flare both in the microwave and hard X-ray domains. Emissions exceeding 300 keV have been imaged in very few flares, while 300–800 keV emission was well pronounced during one of the peaks of the flare under discussion. The sources of such high-energy emissions have been mapped in only few events so far; the 17 June 2003 flare is one such event.

This event is exceptional in being spatially extended and affording an opportunity to measure the HXR spectra of several distinct features in several different light-curve peaks up to several hundred keV, and to compare with radio spectra: this allows us to address aspects of the acceleration mechanism.

We use the following notations for the power-law spectral indices:  $\delta$  corresponds to the electron number,  $\gamma$  corresponds to hard X-ray photons,  $\alpha$  corresponds to microwave flux densities, and  $\alpha_T$  corresponds to microwave brightness temperatures.

## 2. Observations

The event was well observed by RHESSI and other instruments such as the Transition Region and Coronal Explorer (TRACE, Handy *et al.*, 1999) at 1600 and 195 Å. The Michelson Doppler Imager (MDI, Scherrer *et al.*, 1995) on SOHO has provided magnetograms and continuum images close to the event occurrence. RHESSI hard X-ray images are available from about 22:22 (all times hereafter are UT). The event was also observed in soft X-rays by GOES/SXI and in the  $H\alpha$  line in Big Bear. The event started with a filament eruption observed in

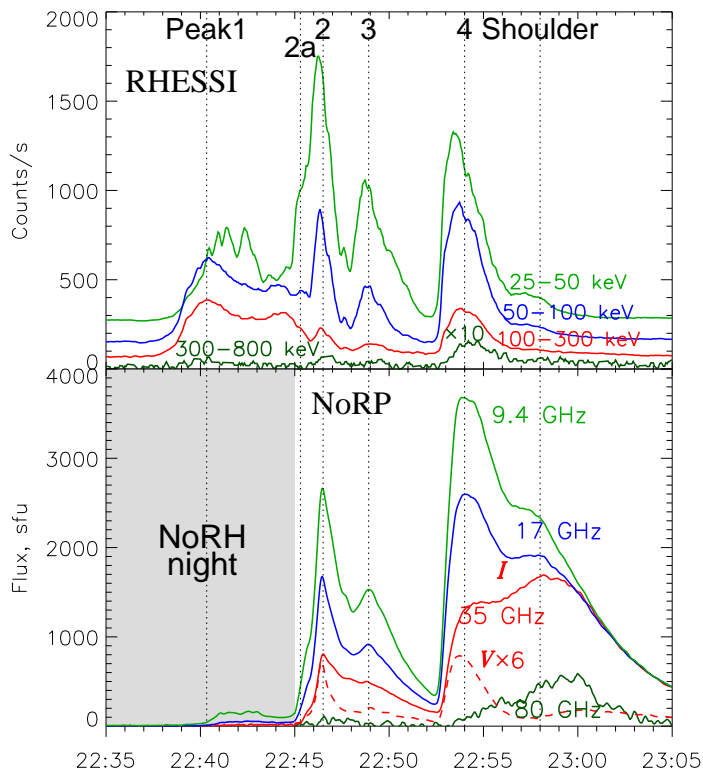


**Figure 1.** RHESSI hard X-ray (top) and NoRP microwave (bottom) total flux time profiles. The 300–800 keV band is magnified by a factor of 10. Prominent peaks as well as a later shoulder are denoted for convenience. RHESSI background levels are shifted to show the bursts better. Radio light curves are shown for Stokes  $I$ , and for Stokes  $V$  at 35 GHz only (dashed; magnified by a factor of 6).

extreme ultraviolet (EUV) and  $H\alpha$  (Ji, Huang, and Wang, 2007). The rise phase of the event occurred before NoRH started observing for the day, so radio images are only available from 22:45 onwards. In addition to NoRH, we also have total flux data from the Nobeyama Radio Polarimeters (NoRP, Torii *et al.*, 1979; Nakajima *et al.*, 1985) at seven frequencies – 1, 2, 3.75, 9.4, 17, 35, and 80 GHz. The HXR and microwave light curves are shown in Figure 1. The impulsive rise in hard X-rays above 25 keV begins at 22:38, with steepest rise at 22:39, and the first HXR maximum in the 50–300 keV bands occurs at about 22:40 (with several sub-peaks in the 25–50 keV range).

### 2.1. The Microwave and Hard X-ray Main Phase

In HXR time profiles in the main phase (Figure 1) we discern four distinct peaks 1, 2, 3, and 4. Peak 1 (22:39–22:43) is not observed by NoRH due to night time. The spatial structures observed during an enhancement labeled 2a (22:44:50–22:45:40) that passes into peak 2 differ from those observed during peak 2 itself, and therefore we consider it separately. Peak 2 (22:45:40–22:47:30),

peak 3 (22:48–22:52), and peak 4 (22:53–22:57) are followed by a plateau in the HXR emission profile which we call the shoulder (22:57–23:00) discernible at 25–50, 50–100, and 100–300 keV. The hardest emission ( $> 300$  keV) is mostly faint, becoming well pronounced only during peak 4.

The NoRP patrol time profiles confirm that the true radio onset in microwaves was at 22:39. The radioheliograph at Nobeyama commenced observing at 22:45, starting with the rise of HXR peak 2a. All other peaks are observed by NoRP up to 80 GHz, including the shoulder at the end of peak 4. The microwave time profiles recorded in Nobeyama basically resemble the HXR records, but they are smoother, and their maxima lag behind the HXR peaks by several tens of seconds. This results in a larger overlap of peaks 2 and 3 with respect to hard X-rays. Note that the sharp drop in microwave flux prior to peak 4 indicates that few non-thermal electrons were trapped in the corona after peaks 2 and 3. Another oddity of the light curves is the fact that the 100–300 keV HXR are actually brightest during peak 1, but, *e.g.*, the 17 GHz radio emission is 50 times brighter in peak 4 than in peak 1. The shoulder is more pronounced in microwaves than in hard X-rays, even exceeding peak 4 at 35 and 80 GHz in intensity. The microwave burst is very strong, reaching 3800 sfu at 9.4 GHz, 2600 sfu at 17 GHz, and 1700 sfu at 35 GHz. Also remarkable is the decay after 23:00, when the flux densities at 9.4, 17, and 35 GHz become almost the same.

A strong emission up to  $\approx 600$  sfu is also recorded at 80 GHz. Measurements of the flux density at 80 GHz from NoRP records are complicated by the following circumstances. A polarization switch of the 80 GHz radiometer degraded for several years until the problem was fixed on 23 June 2005. Accordingly, the flux values at 80 GHz measured between June 1999 and 23 June 2005 gradually decreased with respect to their true values. To repair the 80 GHz flux density, a time-dependent correction factor was inferred from several calibrations (H. Nakajima, 2006, private communication):

$$k_{\text{cor}}(80 \text{ GHz}) = [T_{\{\text{year}\}}/1995.83]^{630}. \quad (1)$$

The accuracy of the corrected total fluxes at 80 GHz within this time interval is considered to be  $\pm 40\%$ , and polarization measurements are not reliable. Data at 35 GHz and, especially, 80 GHz are affected by atmospheric absorption. Uncertainties of the background level contribute to measurement errors. All these factors decrease the measurement accuracy at high radio frequencies.

The flux density at 9.4 GHz surpasses the fluxes at higher frequencies during all peaks in the impulsive phase. The excess of the 9.4 GHz emission is often considered as an indication that the peak frequency of the flaring microwave sources is  $< 17$  GHz, and hence both 35 and 17 GHz emissions are believed to correspond to the optically thin regime. However, this indication could be misleading, as we show later.

## 2.2. The Flare Configuration

### 2.2.1. Flare Ribbons and HXR Sources

This flare occurred in a region which in white light (WL) consisted of a complex of sunspots with strong umbrae and penumbrae. We use TRACE 1600 Å images

to outline the flare ribbons. The TRACE absolute pointing coordinates have an uncertainty significantly larger than its spatial resolution of  $1''^1$ , whereas those of RHESSI are more accurate. For this reason, coordinates in all figures are referred to the RHESSI coordinates. To co-align the TRACE and RHESSI images, we compared the TRACE WL images with full-disk MDI images. Solar rotation was compensated through a re-projection of the continuum images to the same time (analogous routines were performed with MDI magnetograms). Residual inaccuracies of a few arc seconds are possible.

Figure 2 outlines the flare configuration. The TRACE 1600 Å images show the flare ribbons at peak 3 (a) and late in the decay phase (c). Their contours are also overlaid on top of TRACE WL images observed at nearly the same times (e, f). The RHESSI 12–25 keV and 50–100 keV images observed at peak 3 are presented in panel (d), and the contours of the same 50–100 keV images are shown on top of the TRACE WL image (e). Panel (f) shows the TRACE WL decay-phase image as grayscale background along with flare ribbons and oval black/white dashed contours of the RHESSI 100–200 keV images observed at peak 4.

Although the configuration looks like a two-ribbon flare (Ji, Huang, and Wang, 2007), the situation is not quite the classic scenario. Unlike an ordinary flare, the ribbons in this event cross and almost cover sunspots N1 and S2. The emission of the ribbons is faintly visible in the WL image in Figure 2e. Panel (b) presents a WL difference image, in which these brightenings are clearly visible. They are most likely due to the leakage of UV emissions in the TRACE wide-band continuum channel; alternatively, they may show weak white-light emission (*cf.* Metcalf *et al.*, 2003; Hudson, Wolfson, and Metcalf, 2006). The HXR sources also appear to be located within sunspots (N1 and S2), overlapping with their umbrae. Besides the main sources associated with sunspots N1 and S2, there is an additional HXR source south of S2 denoted “SR”.

### 2.2.2. Overall Description of the Event

Having discussed the flare configuration and its main characteristics, we now consider the development of the event from its start up to the late decay. Coronal phenomena are shown by TRACE 195 Å images in Figure 3a–c as well as an H $\alpha$  image in panel (d). A more detailed information is presented by a movie TRACE\_RHESSI.mpeg accompanying the electronic version of our paper, which shows a movie composed of the TRACE 195 Å images overlaid with RHESSI 12–25 keV (red) and 50–100 keV (green) contours.

A system of filaments (F1, F2, F3) covered the whole pre-event region with their northern ends being rooted approximately between N1 and S1 and the southern ends somewhere near SR. One of the filaments (F1) activates at about 22:23, which is manifest in its brightening, and starts to gradually rise (Figure 3a). The activation probably also involves filament F2. This time corresponds to the earliest detectable increase of the soft X-ray flux recorded with GOES

---

<sup>1</sup>see <http://trace.lmsal.com/Project/Instrument/cal/pointing.html> and <http://trace.lmsal.com/tag/>

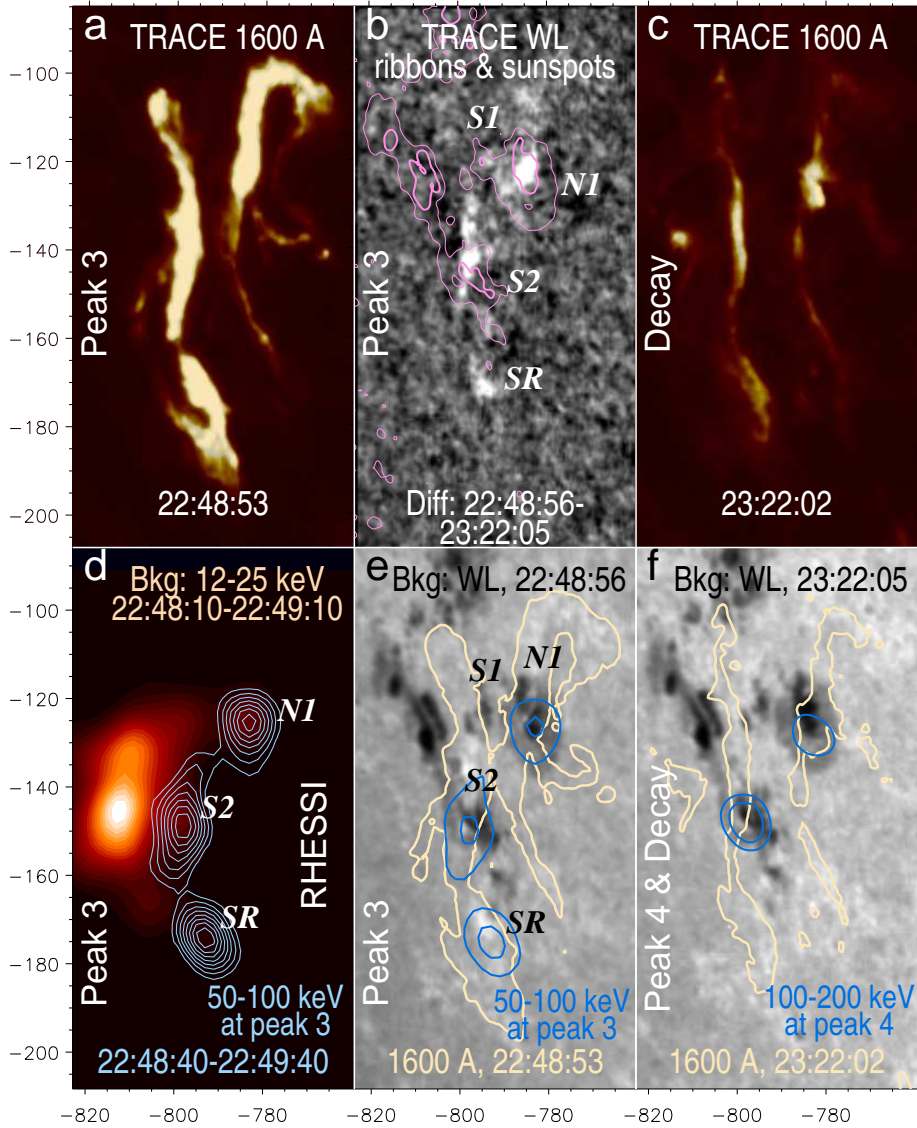


**Figure 2.** Flare ribbons, HXR sources, and sunspots. Ribbons were observed by TRACE during peak 3 (a, b, e) and late in the decay phase (c, f) in the 1600 Å images (a, c) and WL ones (b, e, f). Panel (b) shows a WL difference image with pink contours of the sunspot umbrae and penumbrae. The lower row also shows RHESSI images at peak 3 (d, e; 50–100 keV) and peak 4 (f; 100–200 keV). Levels of blue contours in panels (e, f) are 40% and 80% of the maximum. Yellow contours in panels (e) and (f) correspond to the closest 1600 Å images (a and e). “N1”, “S1”, and “S2” denote major sunspots related to the flare site according to their polarities, and “SR” denotes the southern region of the flare. Axes show hereafter arc seconds from the solar disk center according to the pointing of RHESSI and MDI.

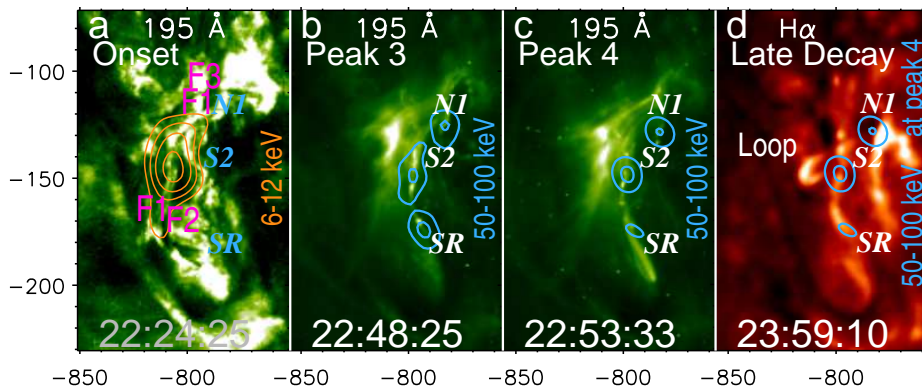


**Figure 3.** Coronal images of the event from the onset up to its late decay: (a): activation of filaments, (b, c): peaks 3 and 4, (d): late decay. Green background shows TRACE 195 Å images in panels (a–c), and red background shows a BBSO H $\alpha$  image in panel (d). Contours show RHESSI images. Labels “N1”, “S2”, “SR” denote flare regions. Filaments visible in TRACE images are labeled “F1–F3” in panel (a). A late-stage H $\alpha$  image (d) shows a post-flare loop between N1 and S2.

monitors (the onset of the event in soft X-rays was reported to be at 22:27). The brightening of the filament indicates heating up to coronal temperatures, while RHESSI shows the presence of still hotter plasmas in this region. The coronal X-ray source detectable up to 25 keV is arranged along the brightening filament.

Then the filaments straighten, rise, and finally erupt (between 22:39:25 and 22:40:40), while their southern ends remain fixed in the position close to the future southern flare region SR (Figure 3b). Note that the first HXR peak occurs simultaneously with the filament eruption. The flare sources N1 and SR are obviously associated with the positions of the ends of pre-eruptive filaments.

The TRACE 195 Å images obtained at peaks 3 and 4 (Figure 3b, c) show a typical arcade of flare loops arranged along the former position of the erupted filaments. The arcade does not exhibit any conspicuous features. The most noticeable are bright kernels in its base which coincide or almost coincide with the HXR sources. H $\alpha$  images obtained late in the decay phase of the event sequentially show cooling post-flare loops. Remarkable is a loop between N1 and S2 caught in an image shown in Figure 3d (the outer edge of its northern leg is already getting dark, while the whole loop remains semi-transparent).

### 2.2.3. Hard X-Ray Morphology

In hard X-rays, the time profile of the flare shows the usual gradual behavior below 25 keV and multiple impulsive spikes at higher energies. The images in the lower energy bands for 6–12 and 12–25 keV, most of which we do not present, show that the flaring region consists of, with a few exceptions (22:52:40–22:55:00), compact sources with apparent flux maxima at  $\sim$  22:46–22:51 and 22:54–22:55. The gradual profile continues until the end of RHESSI sunlight at 23:06. At these low energies, except from 22:52 to 22:55, one does not see footpoint-like compact sources — only a loop-like structure. In the higher energy



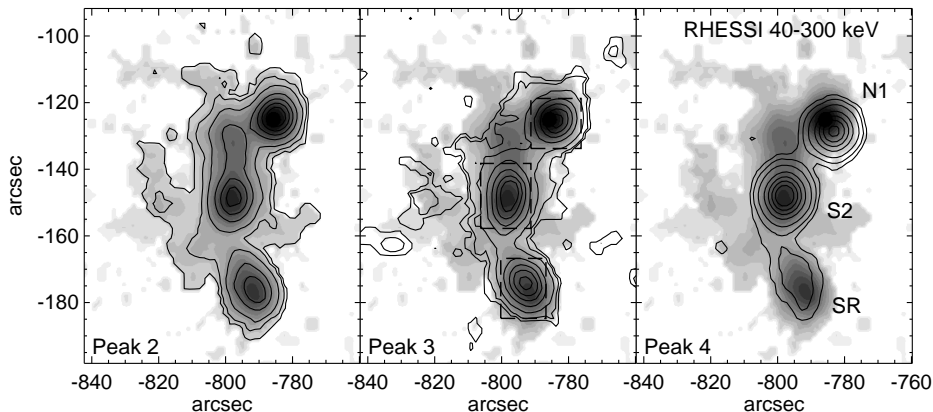


**Figure 4.** Hard X-ray images at each of the three main peaks in the HXR light curve (contours). The images result from summing over the 40–300 keV range. The background image in each panel is the image for peak 2 so that changes in morphology from one peak to the next can be seen. Contours are at 4, 8, 16, 32, 48, 64, and 80% of the peak in each image. The resolution of the images is  $9''$ . The middle panel shows the regions used for the HXR spectra of sources S2, N1, and SR as dotted boxes.

channels, above 40 keV, right from the beginning the main flaring region is resolved into three or more individual compact sources.

The HXR count rate profiles at 25–50 and 50–100 keV of the impulsive phase show four peaks labeled 1, 2, 3, and 4 in Figure 1. Each of these has a different morphology, spectrum, and temporal behavior. To obtain a coherent perspective, we studied the morphology and spectra for each of these. In each case we overlaid the HXR sources on an MDI magnetogram made at the start of the flare. The main result that comes out of this morphological study is that at lower energies one sees the entire flaring loops, including in some cases the loop tops. At higher energies one sees the footpoint sources. This is especially true for peaks 2, 3, and 4 (in peak 1 we see HXR emission close to sunspot S1 that does not recur in the later peaks). An example is shown in Figure 2d for peak 3. Figure 4 also shows the morphology of peaks 2, 3 and 4 in the 40–300 keV range. Hard X-rays of hundreds of keV are seen over most of the length of the flare ribbons, with an extent of almost 60000 km north–south. Three main sources at S2, N1 and SR are prominent in all three peaks, but there are changes in morphology: in particular, peak 2 shows extended emission while peak 4 is dominated by compact sources at S2 and N1. The HXR peak over N1 shifts about  $5''$  to the south-west as the flare evolves from peak 2 to 3 to 4, whereas the S2 source appears at the same location in each peak.

#### 2.2.4. Radio Sources

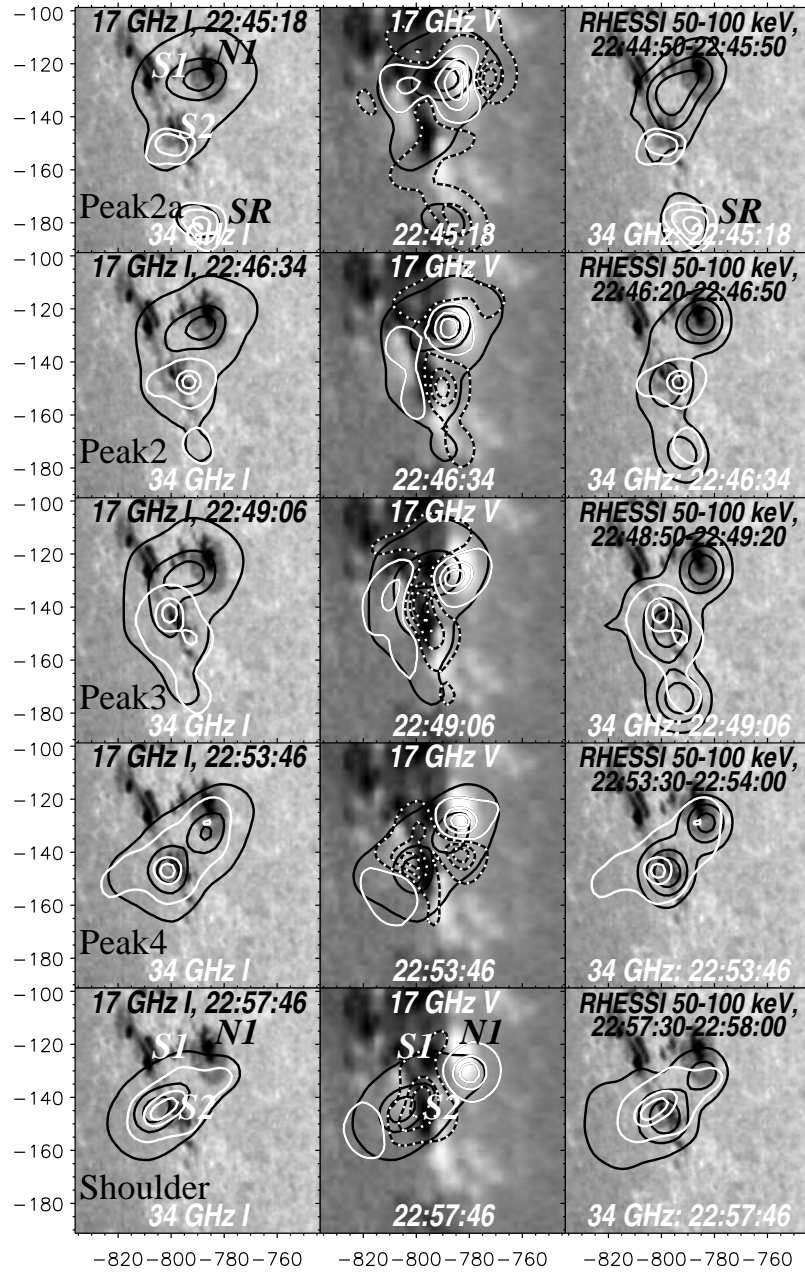
NoRH images at 17 and 34 GHz were synthesized using the NRAO AIPS package. The images were restored with gaussian beams of full-width-half-maximum  $12''$  at 17 GHz and  $8''$  at 34 GHz. At high flux levels the NoRH calibration is established by using the NoRP total flux records.

The co-alignment of microwave sources with other images is not a simple task. The coordinates of the NoRH images are generally found by fitting for the position of the quiet solar disk, but this is not always feasible when the flare flux much exceeds the disk flux. Therefore, when the uncertainties of computations of the solar disk's position are large, the positional accuracy of the NoRH images is poor. They can also suffer from relative shifts. The accuracy of the co-alignment can be improved by referring to some features in other images, *e.g.*, by comparing the radio polarization with a magnetogram. Microwave flare emissions are usually dominated by gyrosynchrotron emission from power-law electrons, which can be significantly polarized in the sense of the  $x$ -mode emission at optically thin frequencies. Thus, the sign of the radio polarization coincides in this case with the polarity of the magnetic field. At frequencies below the turnover of the spectrum, where the emission is optically thick, the radio polarization significantly decreases, and its sign changes to the  $o$ -mode. Taking account of these circumstances, we co-aligned the NoRH 17 GHz maps with the magnetogram and HXR images. The residual inaccuracy might exceed a few arc seconds. The NoRH images at 17 GHz are shown in Figure 5 in the left column (Stokes  $I$ ) on top of the TRACE WL image and in the middle column (Stokes  $I$  and  $V$ ) on top of the pre-event MDI magnetogram.

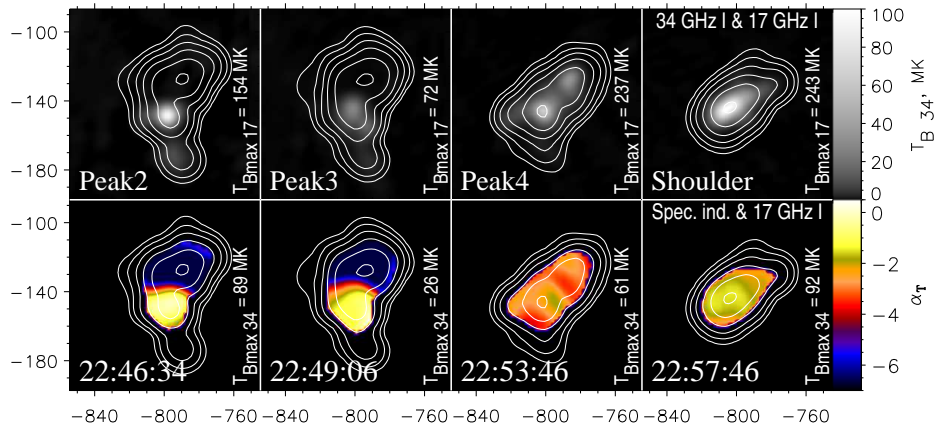
The accurate co-alignment of the 34 GHz images is still more problematic. NoRH does not provide images of the polarized component at 34 GHz. To find the correct positions of the 34 GHz sources, one has to compare their shapes with those at 17 GHz or HXR. The 34 GHz images are shown in Figure 5 in the left and right columns. The absence of 34 GHz emission from the region of the strongest 17 GHz emission over N1 in the three upper rows is surprising, but after a careful analysis of the time sequence of images at both 17 and 34 GHz and in HXR we are confident that the co-alignment is correct to within a few arc seconds.

Figure 5 shows microwave sources at 17 and 34 GHz (NoRH) and RHESSI 50–100 keV images on top of the decay-phase TRACE image (left and right columns) and an MDI magnetogram (middle column). The maximum brightness temperatures in the images are shown in Figure 6 (for 17 GHz in the top row and for 34 GHz in the bottom row). The areas of the microwave sources measured at peak 4 are as follows. The areas of the main 17 GHz sources are 207 arcsec<sup>2</sup> ( $1.1 \times 10^{18}$  cm<sup>2</sup>) in sunspot N1 and 162 arcsec<sup>2</sup> ( $8.8 \times 10^{17}$  cm<sup>2</sup>) in sunspot S2; the areas of the 34 GHz sources are 36 arcsec<sup>2</sup> ( $2 \times 10^{17}$  cm<sup>2</sup>) in sunspot N1 and 108 arcsec<sup>2</sup> ( $5.9 \times 10^{17}$  cm<sup>2</sup>) in sunspot S2.

Starting from the onset of observations in Nobeyama, the 17 GHz emission is dominated by sunspot N1; some contribution from S1 and S2 is also detectable. A similar picture is shown by hard X-rays. In addition, there is a detectable HXR emission from the southern region SR. Unlike the 17 GHz emission, the 34 GHz sources are concentrated in sunspot S2 and SR. From the enhancement 2a to peak 2 and then to peak 3, the source above sunspot S2 increases in intensity, while the HXR emission in S1 relatively decreases. At peak 4 and later on, sunspot S2 dominates, and the strongest emissions come from its umbra, while the sources in sunspot N1 shift south, into its penumbra.



**Figure 5.** Flare morphology observed during peaks 2a–4 and shoulder (consecutive rows). Left column: overlays of 17 GHz (black) and 34 GHz (white) contour maps on a TRACE WL image observed at 23:22:02. Middle column: 17 GHz Stokes  $V$  maps (white; solid positive, broken negative) and Stokes  $I$  maps (black) on an MDI magnetogram observed at 22:23 (bright N, dark S). Right column: RHESSI 50–100 keV (black) and 34 GHz contour maps on the same TRACE WL image as in the left column.



**Figure 6.** Microwave images and spectral indices. 34 GHz images (top row) and spectral indices (bottom row, derived after convolving the 34 GHz images to the 17 GHz resolution) both overlaid by contours of 17 GHz images. Contour levels in each image are at 0.9 of its maximum divided by powers of 3. Scale bars on the right quantify the grayscale and color representations. The maximum brightness temperatures over each image are specified in the upper row for 17 GHz and in the lower row for 34 GHz.

During peak 2 the southernmost flare source denoted “SR” is well pronounced in hard X-rays, but weak at 17 GHz, obviously due to significantly weaker magnetic fields in this region (the microwave intensity is determined by the magnetic field strength). Unlike the sources above sunspots N1 and S2, the source in SR is localized above a bipolar magnetic region. The magnetic field strength in this region varies from  $-770$  G to  $+900$  G under the HXR source.

The magnetic field strengths on the photosphere were measured from full-disk MDI magnetograms. Note that the MDI magnetograms were recalibrated late in 2007, which resulted in an increase of the magnetic field strengths by a factor of about 1.7 (see <http://soi.stanford.edu>). In addition, the position of the active region far from the solar disk center (S08 E58) causes a projectional reduction of the magnetic field strength. Its correction is generally questionable, because the direction of the magnetic field vector might be different. However, we are dealing with main flare sources associated with sunspots, where the magnetic field is nearly radial, and a radialization correction appears to be justified. We have done this by using the *zradialize* SolarSoftware routine. The radialization factor is from 1.82 in N1 up to 1.93 in S2. The maximum magnetic field strength measured from the projection-corrected magnetograms is  $+3080$  G and  $-2120$  G in sunspots N1 and S2 associated with major microwave sources, respectively. The maximum strength in sunspot S1 is  $-1750$  G.

The microwave polarization is of special interest. It corresponds fairly well with the magnetogram. The degree of polarization in N1 initially reaches 50% at peak 2a, and then mostly persists at a level of about 30%. The degree of polarization in S2 is 20–30% throughout the event. However, the contours of the polarization do not perfectly correspond to the magnetic polarity everywhere. The most conspicuous are discrepancies at peak 2a–2 in the region of the main source (N1) and both north and south of it. The polarization structure varies

greatly at this time. Similarly, discrepancies are observed at peak 4 and the shoulder northeast and southwest of S2. It is not possible to explain the discrepancies between the microwave polarization and the magnetogram by insufficient spatial resolution only; certainly there are changes from the  $x$ -mode to the  $o$ -mode emission. This fact hints at a possibility that the 17 GHz emission might not be optically thin.

To check for this possibility, we show in Figure 6 the 17 and 34 GHz Stokes  $I$  images (top row) and a microwave spectral index computed from the spatial distributions of the brightness temperatures at these frequencies (bottom row). The hardest optically thin microwave index  $\alpha_T$  is  $-3.5$  for the hardest realistic power-law index of the electron number spectrum  $\delta = 3$  ( $\alpha_T = 1.22 - 0.9\delta - 2$ , Dulk and Marsh, 1982). As we will see below from HXR spectra, in this event  $\delta > 4$ , and  $\alpha_T < -4.4$ . Thus, orange, brown, and yellow regions are certainly optically thick at 17 GHz; moreover, it is possible that blue regions only are optically thin.

A movie `overlay_wl_17.gif` accompanying the electronic version of our paper shows the radio blob superimposed on the sunspot complex. The main point here is that the flaring source at 17 GHz covers the sunspot umbrae considerably. This is one of the important characteristics of this flare, and may give rise to some of the peculiar features of the event.

From this morphological study one sees that strong X-ray and microwave flare emissions are radiated by a few loops, some of which are rooted in sunspots. A loop between N1 and S1 is detectable during peaks 2 and 3 and, especially, enhancement 2a before them. The southern region SR probably also has a loop structure and is connected with N1. Emissions during peak 4 and the shoulder are dominated by a loop between N1 and S2. Both the microwave and HXR sources have similar structures at this time. The most important point to note here is that the flaring source during peak 4 occurs just above sunspot umbrae. While footpoints mainly radiate at 34 GHz and in HXR, emissions of the whole loops are also detectable at 17 GHz.

### 2.3. Spectral Data

In order to investigate the non-thermal electron energy spectra at different locations in the flare volume, images were made at a range of energies in a number of time intervals. Computations of HXR spectra are complicated by several changes of the RHESSI attenuator and decimation states, and possible time variation in the background. We use both fits to the image data and the standard background-subtracted data analysis to investigate the HXR photon spectra. Images were deconvolved with both CLEAN and Pixon methods for comparison. Since the non-thermal part of the spectra is our major interest, we mostly consider spectra above 40 keV.

Spectra derived from the image cubes in the range 40–240 keV with 20 keV bins are shown in Figure 7 for each of the sources S2, N1, and SR at each of the peaks 2, 3, and 4. Photon power-law indices  $\gamma$  derived from these spectra, and from the RHESSI front detectors (spatially integrated and background-subtracted), are listed along with uncertainties in the fits to the spectra in Table 1.

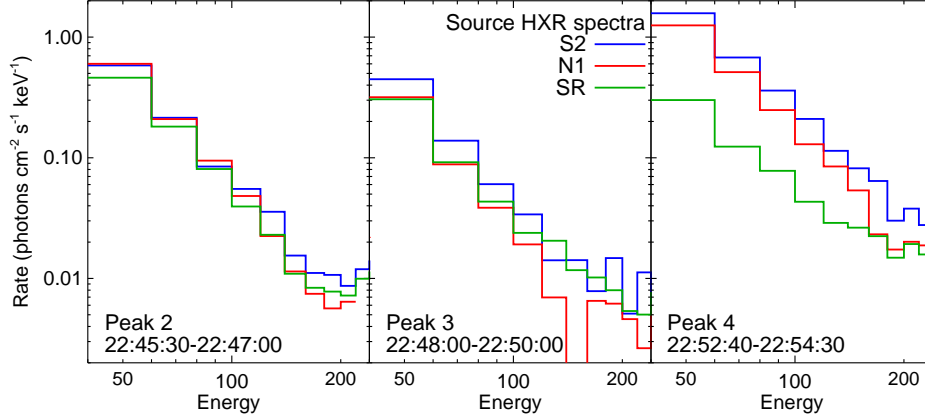


**Figure 7.** Hard X-ray spectra at each of the three main peaks in the light curve for each of the three sources in the HXR images. These are derived from image cubes made in 20 keV channels from 40 to 300 keV.

**Table 1.** Power-law fits to the photon spectral index  $\gamma$  of individual sources in each of the three main peaks in the 17 June 2003 light curve derived from images in different energy bins, together with the fit to background-subtracted 50–400 keV spectra from the RHESSI front detectors. For the spatially integrated spectra, the numbers are the results of a broken power-law fit: the spectral index at energies below the break, the break energy (keV) in parentheses, and the spectral index above the break. Uncertainties in the fits to the break energies are typically large (tens of keV).

Peak	S2 (middle)	N1 (north)	SR (south)	Spatially integrated
2: 22:45:30-22:47:00	$3.1 \pm 0.3$	$3.3 \pm 0.3$	$3.0 \pm 0.4$	3.3 (280) $2.5 \pm 0.2$
3: 22:48:00-22:50:00	$3.3 \pm 0.1$	$3.5 \pm 0.1$	$2.8 \pm 0.5$	3.4 (210) $2.0 \pm 0.2$
4: 22:52:40-22:54:30	$2.7 \pm 0.1$	$2.9 \pm 0.2$	$2.1 \pm 0.6$	2.5 (120) $3.4 \pm 0.2$

The fits to the spatially-resolved spectra assume a single power law over the 40–240 keV range, while the fits to the integrated spectra assume a broken power law over the range 50–400 keV. For peaks 2 and 3 the spectral break in the power law is above 200 keV and the fitted spectral index below 200 keV generally matches the fits to the spatially resolved spectra, which are dominated by photons below 120 keV, while the fit above the break gives a flatter spectrum. However for peak 4 the spectral break is fitted to be at 120 keV: below this energy the spectral index  $\gamma$  is 2.5 while at higher energies it is 3.4. The spatially resolved spectra at peak 4 are consistent with an index of 2.5, as expected since they are dominated by the 40–120 keV photons. There is a suggestion that the spectrum of source SR is somewhat harder than sources S2 and N1 during peak 4, but it is much weaker than those sources and the uncertainty in the spectral index of SR is large (Table 1).

The general conclusion of Figure 7 and Table 1 is that a given peak shows the same energy spectrum in all three spatial locations, but it may differ from one peak to the next: peaks 2 and 3 clearly have steeper spectra than peak 4 (below 120 keV) in all three sources and in the integrated spectra. This suggests either

that the electron acceleration mechanism has the same physical characteristics over a large spatial scale ( $5 \times 10^5$  km) or a more localized accelerator distributes electrons over the full volume. The challenge for the first interpretation is the fact that all sources show a flattening of their spectra in peak 4 after being steeper in peaks 2 and 3: how can sources so far apart have their characteristics change in the same way? For example, if acceleration is due to stochastic acceleration by wave turbulence, how is turbulence generated with identical properties over such a large volume? On the other hand, a localized accelerator that can distribute non-thermal electrons over a distance of  $5 \times 10^5$  km is difficult to reconcile with the usual picture of post-flare loops in two-ribbon flares that are typically much shorter than the ribbons and straddle the neutral line rather than parallel the ribbons.

Peak 2 is of special interest, because at this peak we have encountered a puzzling situation with no 34 GHz emission from the region of the 17 GHz source at N1. Such a situation is possible if the 17 GHz emission is thermal gyroresonance emission at low harmonics of the gyrofrequency. However, the first panel of Figure 7 clearly shows that the HXR spectrum of N1 in the first peak does have non-thermal photons up to 200 keV that must result from electrons with energies of order 500 keV or more.

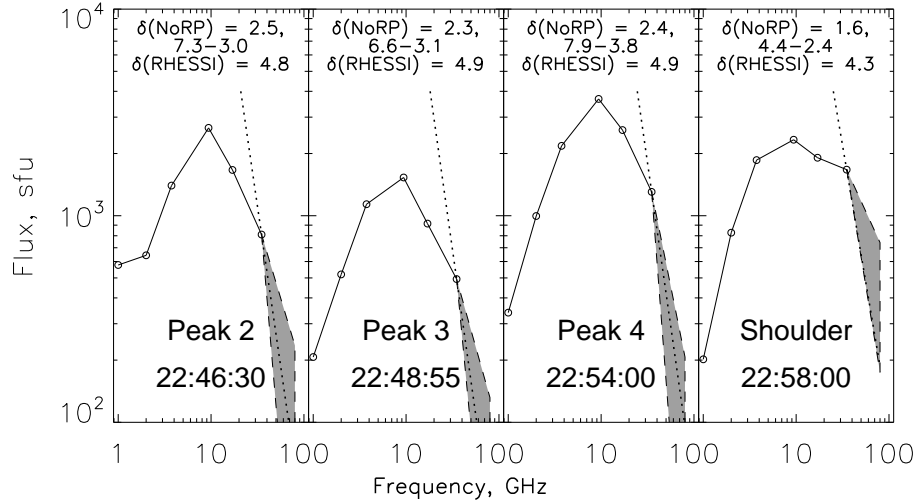
### 2.3.1. Microwave Spectra

Figure 8 shows the microwave spectra at four different epochs — peaks 2, 3, 4, and the shoulder, using the NoRP frequencies at 1.0, 2.0, 3.75, 9.4, 17, 35, and 80 GHz. All spectra show distinct maxima at about 10 GHz with the exception of the shoulder which seems to have a complex spectrum, with two peaks:  $\nu_{\text{peak 1}} \approx 10$  GHz,  $\nu_{\text{peak 2}} > 20$  GHz. The thick dotted lines in all panels show the highest-frequency slope  $\alpha = 1.22 - 0.9 \delta_{\text{RHESSI}}$  corresponding to the RHESSI spectrum ( $\delta_{\text{RHESSI}} = \gamma + 1.5$ ).

The shapes of the spectra imply non-thermal emission for all four epochs shown in the figure. Recalling that the microwave flux densities become almost the same during the decay (see Figure 1), it is useful to compare their values with estimates from soft X-ray observations.

From RHESSI 6–12 keV images at 22:53–22:57 we find the SXR-emitting area to be  $A \approx (2 - 6) \times 10^{18}$  cm<sup>2</sup> (levels of 0.3–0.6 of the maximum), and a volume  $\sim A^{3/2} \approx (4 - 13) \times 10^{27}$  cm<sup>3</sup>. From a thermal component fit to the RHESSI spectrum below 50 keV at 22:58 we find an emission measure of  $2.8 \times 10^{49}$  cm<sup>-3</sup> and a temperature of 20 MK. For comparison, we estimated the temperature and emission measure variations throughout the event from GOES-12 soft X-ray fluxes assuming coronal abundances (White, Thomas, and Schwartz, 2005). At the same time of 22:58, these estimates provide an emission measure of  $3.5 \times 10^{49}$  cm<sup>-3</sup>, density of  $(5 - 10) \times 10^{10}$  cm<sup>-3</sup>, and temperature of 15 MK — reasonably close to the estimates from RHESSI data. The thermal radio flux estimated from SXR data is maximum at 22:58 and does not exceed 28 sfu. Thus, non-thermal emissions appear to dominate all the microwave/millimeter sources throughout the event.

The slopes of the microwave spectra between the highest frequencies of 35 and 80 GHz are very uncertain but do not seem to be inconsistent with electron



**Figure 8.** Microwave spectra. Shadings show the uncertainties of the flux density at 80 GHz. The spectral indices  $\delta_{\text{NoRP}}$  specified in panels a–d were calculated from the flux ratios at 17 and 35 GHz (upper row) as well as from the flux ratios at 35 and 80 GHz at the lower and upper boundaries of the shaded regions, respectively. The thick dotted lines show the highest-frequency slope corresponding to the RHESSI HXR spectrum in the energy range 100–300 keV produced by MeV electrons.

spectrum power-law indices inferred from the HXR photon energies in the range 100–300 keV. The slopes between 17 and 35 GHz are significantly flatter than the spectra of the HXR-emitting electrons, with a difference of 2.3–2.7. This fact is consistent with our preliminary assumption that the 17 GHz emission is not optically thin, although the peak frequency of the microwave total flux spectrum is at about 10 GHz for the most part of the event.

### 3. Modeling and Estimates

#### 3.1. Microwave/Millimeter Emissions

To compare the microwave parameters with parameters inferred from HXR spectra, we use the expressions employed by White *et al.* (2003) [based on Hudson, Canfield, and Kane (1978)] for the 23 July 2002 flare. For a measured photon spectrum of thick-target non-thermal bremsstrahlung of the form

$$\Phi(E_\gamma) = A_0 \left( \frac{E_\gamma}{E_0} \right)^{-\gamma} \text{ [photons keV}^{-1} \text{ cm}^{-2} \text{ s}^{-1}] \quad (2)$$

where  $E_\gamma$  is the photon energy,  $\gamma$  is the power-law index of the photon spectrum, and  $A_0$  is the normalization constant at a fiducial photon energy  $E_0$  keV ( $A_0 = 50$  keV in the OSPEX software used to fit the RHESSI spectra), the energy



distribution of non-thermal electrons takes the form

$$\frac{d^2N(E)}{dEdV} = N_r \frac{\delta - 1}{E_r} \left( \frac{E}{E_r} \right)^{-\delta} \quad (3)$$

(number of electrons of energy  $E$  per unit volume and energy) where  $\delta = \gamma + 1.5$ ,  $E_r$  is a reference energy (typically 10 keV), and

$$N_r = 3.04 \times 10^{24} \frac{A_0 b(\gamma)}{(\delta - 1) E_0^{0.5} A_X} \left( \frac{E_0}{E_r} \right)^{\delta - 1} \text{ [electrons cm}^{-3}\text{]} \quad (4)$$

Here  $b(\gamma) = \gamma^2(\gamma - 1)^2 B(\gamma - 0.5, 1.5)$  where  $B(x, y)$  is the beta function, and  $A_X$  is the area of the HXR source.

The parameters of the electron energy distribution may be used to calculate the expected microwave emission due to the gyrosynchrotron process. There is no simple exact expression for this calculation, but Dulk and Marsh (1982) provide simple approximations. The power-law index of the microwave total flux spectrum in the optically thin limit,  $\alpha$ , is related to the power-law index of the electron number spectrum by  $\alpha = 1.22 - 0.9 \delta$  (Dulk and Marsh, 1982). With these expressions it is possible to compare quantitatively the observed photon HXR spectra with the microwave spectra.

### 3.1.1. Emissions from N1 during Peak 2

As mentioned, the absence of emission at 34 GHz in the source above sunspot N1 during Peak 2 might be explained if the 17 GHz emission is due to a thermal gyroresonance source. As Figure 7 shows, the HXR spectrum in source N1 is detectable up to at least 200 keV. Fits to the photon spectrum show a power-law with  $\gamma = 3.3$ , but rule out a high-temperature thermal component.

Estimations of the non-thermal gyrosynchrotron emission from power-law electrons with  $\delta = \gamma + 1.5 = 4.8$  using formulas of Dulk and Marsh (1982) show that the observed 17 GHz emission above N1 (150 MK) is possible. The ratio of the brightness temperatures at 34 and 17 GHz is  $T_{34}/T_{17} \approx (34/17)^{(1.22 - 0.9\delta - 2)} \approx 0.029$ , and the brightness temperature expected at 34 GHz in N1 should be about 4.4 MK. The maximum brightness temperature observed at 34 GHz at peak 2 is about 90 MK in S2; the dynamic range should be sufficient to detect a 4.4 MK source (5%, or  $-13$  dB). It is not clear why the 34 GHz emission is absent in N1, if the emission is non-thermal.

A possible solution of this problem is a power-law-like spectrum with an upper cutoff at a few hundred keV. The number of moderate-energy electrons is sufficient to produce the observed strong 17 GHz emission — even a thermal spectrum would suffice. However, the deficiency of higher-energy electrons probably determines the absence of the 34 GHz emission.

### 3.1.2. Emissions during Peak 4

Having parameters of the HXR spectra, one can estimate parameters of the radio emission. Calculations of radiation of electrons gyrating in magnetic fields (*e.g.*,

Ramaty, 1969; Ramaty *et al.*, 1994; Preka-Papadema and Alissandrakis, 1992; Bastian, Benz, and Gary, 1998) appears to be the most rigorous way. Another way introduced by Dulk and Marsh (1982) uses formal analytic approximations of the rigorous results. The common problem of both methods is that there are large uncertainties of several important parameters; however, the latter method appears to be more flexible, it is not time-consuming, and allows to get estimates easily.

First, we try to estimate the magnetic field strength from the flux density recorded by NoRP at 35 GHz during peak 4 assuming the emission at this frequency to be optically thin (this seems to be correct in our case, *e.g.*, according to Figure 6). Most parameters seem to be known. The area of the thick target measured from RHESSI 25–50 keV images was  $A_X \approx 1 \times 10^{18} \text{ cm}^2$ . We take  $\gamma = 3.4$  [ $\delta = 4.9$ ,  $B(\gamma - 0.5, 1.5) = 0.16$ , and  $b(\gamma) = 10.3$ ],  $A_0 \approx 5.2$  photons  $\text{cm}^{-2} \text{ keV}^{-1} \text{ s}^{-1}$  from the HXR spectrum [see (2)]; derive  $N_r \approx 3 \times 10^9$  from (4); take the geometrical depth of the emitting source to be the square root of its area, and the angle between the line of sight and the magnetic field to be  $\approx 60^\circ$  according to the position of the active region. Assuming the total flux to be contributed by two identical footpoint sources in equal magnetic field strengths, we get  $B \approx 1200 \text{ G}$  from formulas of Dulk and Marsh (1982). This seems to be plausible taking account of the estimates of the photospheric field from the MDI data. With this magnetic field strength, the frequency maximum is  $\nu_{\text{peak}} \approx 30 \text{ GHz}$ , which appears to agree with our preliminary conclusions made in Section 2.2.4, but is well above the peak frequency shown by the NoRP total flux spectrum (9.4 GHz). Another useful quantity is the maximum flux density  $S(\nu_{\text{peak}}) \approx 10^{-19} k_B \nu_{\text{peak}}^2 / c^2 (1 - \exp(-2)) T_{\text{eff}}(\nu_{\text{peak}}) \tau(\nu_{\text{peak}}) \Omega \approx 1140 \text{ sfu}$  where  $k_B$  is the Boltzmann constant and  $\Omega$  is the solid angle of one source visible from the Earth. The peak frequency is shown in Figure 9a by the vertical dash-dotted line, and  $2S(\nu_{\text{peak}})$  is shown by the square. These parameters obviously disagree with the NoRP spectrum (gray). To understand the situation, we model the spectrum of the emitting source at a frequency  $\nu$  as

$$T(\nu) = T_{\text{eff}}(\nu)[1 - e^{-\tau(\nu)}] \quad (5)$$

where  $T_{\text{eff}}(\nu)$  is the effective temperature of emitting electrons,  $\tau(\nu) = \kappa(\nu)L$  is the optical thickness,  $\kappa(\nu)$  is the absorption coefficient, and  $L$  is the geometrical depth. Both  $T_{\text{eff}}(\nu)$  and  $\kappa(\nu)$  are functions of all parameters of the source determined by formulas of Dulk and Marsh (1982).

The spectrum modeled in this way and converted to flux density is shown in Figure 9a by a solid black line. It significantly differs from the NoRP spectrum. One might assume that our extension of the approach of Dulk and Marsh (1982) is not justified, *e.g.*, because we have ignored the fact that the accuracy of their expressions decreases at high ( $> 100$ ) harmonics of the gyrofrequency and at low ( $< 10$ ) ones, with the latter being more important in our case.

To verify our results, we have overplotted in the same figure the spectrum calculated using the Ramaty code (Ramaty, 1969; Ramaty *et al.*, 1994) (dashed line). To co-ordinate the different geometries of the sources used in both ways, we have corrected the normalization coefficient for the Ramaty code by a geometrical factor  $k_{\text{geom}} = 4/(3\sqrt{\pi})$ , so that  $A_{\text{nor}} = N_r \times (\delta - 1) \times (1 \text{ MeV}/E_r)^{1-\delta} ALk_{\text{geom}}$

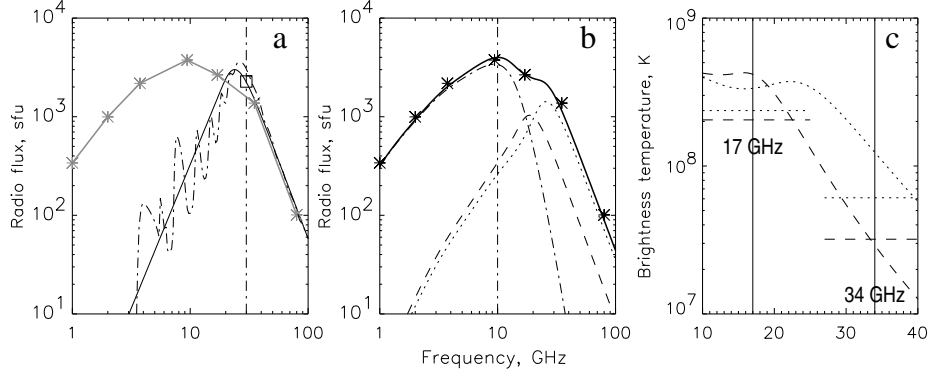


**Figure 9.** Modeling of the microwave spectrum at Peak 4. (a) The observed NoRP spectrum (gray) and the spectra of two identical footpoint sources modeled using the approach of Dulk and Marsh (black solid) and the Ramaty code (dash-dotted). (b) The flux density spectra of the two footpoint sources (dotted and dashed lines) and the looptop part (dash-dotted line), and the total spectrum (thick line). Asterisks in panels (a) and (b) show the NoRP measurements, and the vertical dash-dotted lines mark the turnover frequencies. (c) The spectrum of the brightness temperatures for the footpoint sources. The vertical lines mark 17 and 34 GHz, and the horizontal lines mark the brightness temperatures actually observed in these regions.

$= 1.9 \times 10^{29}$  electrons  $\text{MeV}^{-1}$ . Both model spectra satisfactorily agree with each other—of course, without gyroresonance features in the spectrum modeled following Dulk and Marsh (1982), which are not really expected in observations due to inhomogeneity of the magnetic field. Finally, we note that if asymmetric microwave sources were assumed, then the magnetic field strength (and the turnover frequency) for one of them would be still higher.

From comparing the results of the modeling with the observed spectrum, we conclude that an essential emitting component is missing, which is minor at high radio frequencies but dominates at lower frequencies. Even with a frequency-independent brightness temperature, the area of this component must increase with wavelength to partially compensate the decrease of  $\nu^2$ . Indeed, as known from multi-frequency imaging observations and modeled theoretically, radio-emitting regions expand with wavelength. For example, Bastian, Benz, and Gary (1998) modeled the radio emission of a magnetic loop filled with power-law electrons above a dipole, and the resulting total flux spectrum which they obtained was broadly similar to our situation. Therefore, besides the “kernel” sources emitting at high microwaves and long millimeter wavelengths, there must be a larger blob covering them, with an area and optical thickness increasing with wavelength. We roughly reproduce the results of Bastian, Benz, and Gary (1998) by combining the radio-emitting regions from two kernel sources localized in both footpoints of the loop and a blob above them.

We represent the intrinsic brightness temperature of a single source 1 at a frequency  $\nu$  according to (5), and its issue after the passage through another source 2 as  $\exp(-\tau_2(\nu))$ . Thus, the brightness of a kernel source visible through a blob above it is

$$T(\nu) = T_{\text{eff k}}(\nu) \left[ 1 - e^{-\tau_k(\nu)} \right] e^{-\tau_b(\nu)} + T_{\text{eff b}}(\nu) \left[ 1 - e^{-\tau_b(\nu)} \right]. \quad (6)$$

We force the area of the blob  $A_b$  to depend on frequency approximately according to Bastian, Benz, and Gary (1998) and correspondingly change the depth. The magnetic field is also handled as a growing function of frequency. This approach uses the fact that while the frequency decreases, a source becomes thicker, and the contribution from peripheral regions of weaker magnetic fields grows.

The results of the modeling are shown in Figure 9b. First of all, we warn against overinterpreting these results, because the model is coarse, parameters are not well known, and we therefore did not endeavor to achieve perfect results. The dotted and dashed lines represent the “column” total flux spectra of the two kernel source visible through the loop-associated blob, and the dash-dotted line represents the spectrum of the blob. Panel (c) in the figure shows the brightness temperatures of the kernels. The vertical lines mark 17 and 34 GHz, and the horizontal lines mark the brightness temperatures actually observed in these regions. The relations between the two sources are roughly reproduced at both frequencies, although the brightness temperatures at 17 GHz are higher than the actually observed ones—probably, the sources are not completely resolved at 17 GHz. The flat parts left from the turnover frequencies are due to the contributions from the blob.

We used here  $A_0 = 5.2 \text{ photons s}^{-1} \text{ cm}^{-2} \text{ keV}^{-1}$  from the observed HXR spectrum, the observed areas of the kernel sources (see Section 2.2.4), and the magnetic field strengths of 1350 and 900 G (stronger in S2, because the sources were displaced from N1 during peak 4). Their depths were taken as the square root of the areas. The area of the covering blob varied from  $8 \times 10^{18} \text{ cm}^2$  at 15 GHz up to  $1.5 \times 10^{20} \text{ cm}^2$  at 1 GHz, and its depth was taken to be  $0.2\sqrt{A_b}$ . Accordingly, the magnetic field strength gradually decreased from 540 G to 74 G. Again, we point out that the values of all quantities are estimates only.

With the coarseness of the model, this exercise nevertheless leads to the following reasonable conclusions: (*i*) the broad total flux spectrum could be indeed due to the emission from the whole loop; (*ii*) the peak frequency shown by NoRP does not correspond to real turnover frequencies of the main sources observed at 17 and 34 GHz, being significantly lower; and (*iii*) the parameters of accelerated electrons found from HXR spectra appear to correspond to parameters of microwave-emitting electrons.

Two main results come out from our considerations: (*i*) flaring in strong magnetic fields, and (*ii*) inhomogeneity of a microwave source — in the sense that different parts of a source dominate its emission at different frequencies. The major result of our modeling is a warning for researchers that if the peak frequency observed in the total flux spectrum is relatively low (*e.g.*, 10 GHz), this does not guarantee that sources observed at higher frequencies of 17 GHz or even 34 GHz are optically thin. Our modeling is rather coarse, but it demonstrates anyway that the peak frequency observed in the total flux spectrum can be significantly lower than the peak frequencies in footpoint-associated sources. This conclusion is consistent with the assumption of White *et al.* (2003) and hints at another possible reason for the long-standing discrepancy between the power-law indices estimated from HXR and radio data.

### 3.1.3. The Shoulder and Decay

The behavior of the flux density at long millimeter wavelengths during the shoulder appears to be intriguing (see Figure 1): the shoulder is pronounced only at lower HXR energies ( $< 300$  keV), which do not significantly affect microwaves, and its intensity is substantially lower than peak 4, whereas the opposite situation occurs at 35 and 80 GHz. As the lower row in Figure 5 shows, flaring is mainly concentrated in S2 at that time, which is nearly similar to the situation during peak 4. The electron spectrum becomes slightly harder (4.3 against 4.9 at peak 4), but this does not seem to be sufficient to explain the observations. A possible solution of this problem might be related to trapping effects. Note also that the relation between the power-law electron indices inferred from HXR and microwave spectra observed at peak 4 and the shoulder (see Figure 8) hints at progressive hardening of microwave-emitting electrons with respect to HXR-emitting ones.

Melrose and Brown (1976) in their trap-plus-precipitation model analytically showed that Coulomb collisions in plasma with a density  $n_0$  significantly affect the “parent” power-law electron spectrum with an index  $\delta_{\text{inj}}$  injected into a trap so that the number spectrum of trapped electrons transforms into a two-part one separated by a transition energy  $E_T$ . The  $E_T$  moves right with time  $t$ ; in the non-relativistic limit,  $E_T = (3/2 \nu_0 t)^{2/3}$  with  $\nu_0 \approx 5 \times 10^{-9} n_0 \text{ keV}^{3/2} \text{ s}^{-1}$ . The branches below  $E_T$  and above it depend on the regime of the injection into the trap. Melrose and Brown (1976) considered, in particular, two limiting injection regimes, i.e., an initial impulsive injection and a continuous one. Metcalf and Alexander (1999) presented in their figures 3 and 4 the spectra calculated for these injection regimes with  $\delta_{\text{inj}} = 4$  for a parent spectrum, which is close to our case. Schematically, the effects of trapping are as follows.

After an impulsive injection, the electron number spectrum is depleted to harden so that the upper envelope of the whole spectrum goes as  $\delta_{\text{inj}} - 1.5$ , and the branch below  $E_T$  falls as  $E^{5/2}$  towards lower energies. During a continuous injection, the electron number spectrum is augmented to become a broken double-power-law so that the high-energy branch keeps a slope of  $\delta_{\text{inj}}$  and the low-energy one takes a slope of  $\delta_{\text{inj}} - 1.5$ . The high-energy branch augments linearly with time. The spectrum of the HXR emission produced by electrons precipitating from a trap in the model of Melrose and Brown (1976) is the same as the thick-target spectrum without trapping due to the steeper spectrum of the collisional precipitation from a trap. These effects altogether result in hardening the spectrum of trapped microwave-emitting electrons with respect to HXR-emitting ones (Melnikov and Magun, 1999).

The case of a continuous injection resembles the progressive hardening of microwave emission observed during the shoulder, especially pronounced in the 80 GHz flux starting from peak 4 by 23:00. The trapping seems to be insignificant at the onset of peak 4, because the polarized emission at 35 GHz closely resembles the 100–300 keV light curve (see Figure 1). Then the 80 GHz flux increases almost linearly with time, as expected for a continuous injection in a trap.

An additional support in favor of trapping is provided by a loop-top brightening visible in 34 GHz images obtained during the shoulder and decay (see, *e.g.*,

the upper right image in Figure 6). The flat spectrum at 9.4–35 GHz during the decay might be due to combined effects of trapping and inhomogeneity of the microwave-emitting source. Both trapped and precipitating electrons can contribute to the microwave emission (Kundu *et al.*, 2001) which makes difficult a more detailed analysis of trapping issues in our event due to insufficient information.

#### 4. Discussion and Conclusion

We have analyzed an event which is interesting in many respects. It is one of the few events whose high energy emission in hard X-rays has been mapped above 200 keV; electron spectra inferred from hard X-rays are consistent with those inferred from microwave data, but the latter have very large uncertainties. A distinctive feature of our study is related to strong magnetic fields. The combination of the MDI calibration correction and the assumption of radial fields leads magnetic field strengths three times stronger than uncorrected ones. Such a correction factor appears to be significant for magnetic fields themselves; it becomes rather crucial in the interpretation of the gyrosynchrotron emission. We now illustrate what one would see if the magnetic fields in footpoint sources in the event were thought to be 2–3 times weaker.

1. The underestimation of the magnetic field strength results in an underestimate of the microwave peak frequency; indeed one sees a low peak frequency of the NoRP total flux spectrum. We have shown that this low peak frequency is due to the contribution of emission from the upper blob associated with the whole loop. Thus, the apparent consistency of the low peak frequency with weak magnetic field is in this case deceptive.
2. Consequently, radio frequencies which do not correspond to the optically thin regime can be misinterpreted as belonging to the optically thin regime. There is no reason to use problematic 80 GHz records in this case, and the microwave spectrum estimated from the 35 to 17 GHz ratio inevitably becomes flatter than the optically thin one. The discrepancy with the HXR spectrum then appears naturally.
3. Believing that the 17 GHz emission belongs to the optically thin regime, one gets a strange behavior of the polarization.
4. With the underestimated magnetic field, one gets a significant deficiency of the flux density, and is constrained to search for a way to increase it.
5. The Razin effect seems to become important at higher frequencies than in reality. It was most likely negligible in our event.

These considerations might provide a key to reconcile some puzzling issues established in several other events. As a by-product of our analysis we conclude that the re-calibrated MDI magnetograms appear to be more consistent with microwave data than the previous ones.

Two strong HXR and microwave footpoint sources above sunspots dominated throughout the event. We find that at all peaks the HXR sources had nearly the same positions. The flare source in energy bands from 25 to 400 keV coincided to

within  $1''$  at the onset of peak 4. This suggests that the acceleration process must be the same for all energy levels — from 25 to 400 keV. Grigis and Benz (2008) from their study of the spectral evolution of HXR bursts also concluded that the observed spectral changes occur due to “gradual change in the accelerator” rather than contribution from different acceleration mechanisms. Our results appear to be consistent with this conclusion, although they do not seem to confirm the model proposed by Grigis and Benz (2008).

On the other hand, the HXR spectra differ from peaks 2 and 3 to peak 4. The earlier peaks show a power law with electron index  $\delta \approx 4.9$  from 40 to over 200 keV, with a slightly flatter (but more uncertain due to low count rates) spectrum above the break. Peak 4, on the other hand, shows a flatter spectrum ( $\delta \approx 4.0$ ) below photon energies of 120 keV, with  $\delta \approx 4.9$  above this energy. The important result of spatially resolved spectroscopy in this event is that all three main sources simultaneously exhibit the flattening in the photon energy range 40–120 keV in peak 4: this implies that over the large volume encompassing these sources, the conditions that control the spectral index of accelerated electrons changed simultaneously. This is a severe constraint on acceleration models.

In terms of magnetic reconnection models (*e.g.*, Forbes and Priest, 1995), one might indeed expect the flaring to be strongest above regions of strong, highly sheared magnetic fields, and particularly over the umbrae of delta spots. Several authors (*e.g.*, Qiu *et al.*, 2002; Asai *et al.*, 2004) have reported a correlation between the energy release rate computed from footpoint motions across the magnetic fields and intensities of flare emissions in HXR and microwaves. A similar correlation probably would exist for the event under discussion. However, existing flare models do not seem to predict the various properties of the flare revealed in our paper, *e.g.*, whether a flare would enter a sunspot, how hard the electron spectrum could be, *etc.*

A class of flares occurring above the sunspot umbrae does not seem to be sufficiently studied, and their properties have not been well established. Note that the analysis of the extreme 20 January 2005 event led Grechnev *et al.* (2008) to a conclusion that its extremeness was due to the occurrence of the flare above the sunspot umbrae. One of features observed in that flare was a large SXR-emitting loop-like structure rooted in the umbrae. Such a loop between sunspots N1 and S2 was also observed in our 17 June 2003 flare (see Figure 3d). Total magnetic flux was mainly concentrated between two umbrae, unlike widespread magnetic fields in a typical flare. This feature seems to be expected: large total magnetic flux outgoing from a sunspot must be balanced by incoming flux at the other end of a loop that is favored by the presence of another sunspot. However, this is one of only a few expected properties of sunspot-associated flare.

#### 4.1. Summary

Our multi-spectral analysis of the 17 June 2003 event has shown that its main features were probably related to the location of main flare sources above sunspots. This may determine strong microwave flare emissions and probably was somehow related to hard electron spectra observed in the event. Properties of flare emissions imply a single acceleration mechanism, which was most likely the same for

all energy domains up to 800 keV. Some features of microwave emissions appear to be indicative of trapping issues, consistent with existing concepts. We have not found a significant discrepancy between the spectra of electrons responsible for microwaves and hard X-rays frequently reported in previous studies (with the limitation that the microwave index is very uncertain). Instead, we note that sometimes this discrepancy could be due to underestimation of the microwave turnover frequency resulting from inhomogeneity in the microwave/millimeter source. So we emphasize that the microwave peak frequency measured from total flux records does not guarantee that higher frequencies are all optically thin. It rather shows the lower limit of possible turnover frequencies of gyrosynchrotron spectra of footpoint-associated sources. This is also related to probable underestimations of the magnetic field strength. This conclusion appears to be consistent with the results of White *et al.* (2003) which implied an optically thick regime even at 35 GHz, although their event was significantly different. These issues highlight the importance of total flux measurements of radio bursts in the millimeter range. Our results also emphasize the importance of both experimental and theoretical analyses of sunspot-associated flares, which might be related to extreme solar events, but do not appear to be sufficiently studied.

**Acknowledgements** We thank A.M. Uralov, A.T. Altyntsev, and H.S. Hudson for useful discussions. We thank the instrumental teams of the TRACE mission, MDI on SOHO, the Nobeyama Solar Facilities, the Big Bear Solar Observatory, and the GOES satellites. We thank an unknown referee for useful suggestions.

The research of MRK and SMW for this paper was supported by NSF grant ATM 02-33907 and NASA grants NAG 5-12860 and NNG05-GI-91G. The research of EJS was supported by NASA grants NAG 5-10180 and NNG06-GB-636. The research of VVG and NSM was supported by the Russian Foundation of Basic Research under grant 07-02-00101.

## References

- Asai, A., Yokoyama, T., Shimojo, M., Masuda, S., Kurokawa, H., Shibata, K.: 2004, *Astrophys. J.* **611**, 557.
- Bastian, T. S., Benz, A. O., Gary, D. E.: 1998, *Annu. Rev. Astron. Astrophys.* **36**, 131.
- Bogachev, S. A., Somov, B. V.: 2001, *Astron. Lett.* **45**, 157.
- Bogachev, S. A., Somov, B. V.: 2007, *Astron. Lett.* **33**, 54.
- Dulk, G. A., Marsh, K. A.: 1982, *Astrophys. J.* **259**, 350.
- Forbes, T. G., Priest, E. R.: 1995, *Astrophys. J.* **446**, 377.
- Grechnev, V. V., Kurt, V. G., Chertok, I. M., Uralov, A. M., Nakajima, H., Altyntsev, A. T., *et al.*: 2008, *Solar Phys.* **252**, 149.
- Grigis, P. C., Benz, A. O.: 2008, *Astrophys. J.* **683**, 1180.
- Handy, B. N., Acton, L. W., Kankelborg, C. C., Wolfson, C. J., Akin, D. J., Bruner, M. E., *et al.*: 1999, *Solar Phys.* **187**, 229.
- Hudson, H. S., Canfield, R. C., Kane, S. R.: 1978, *Solar Phys.* **60**, 137.
- Hudson, H. S., Wolfson, C. J., Metcalf, T. R.: 2006, *Solar Phys.* **234**, 79.
- Ji, H., Huang, G., Wang, H.: 2007, *Astrophys. J.* **660**, 893-900.
- Kundu, M. R., White, S. M., Gopalswamy, N., Lim, J.: 1994, *Astrophys. J. Suppl.* **90**, 599.
- Kundu, M. R., White, S. M., Shibasaki, K., Sakurai, T., Grechnev, V. V.: 2001, *Astrophys. J.* **547**, 1090.



- Lee, J., Gary, D. E., Shibasaki, K.: 2000, *Astrophys. J.* **531**, 1109.
- Lin, R. P., Dennis, B. R., Hurford, G. J., Smith, D. M., Zehnder, A., Harvey, P. R., *et al.*: 2002, *Solar Phys.* **210**, 3.
- Melnikov, V. F., Magun, A.: 1998, *Solar Phys.* **178**, 153.
- Melrose, D. B., Brown, J. C.: 1976, *Mon. Not. Roy. Astron. Soc.* **176**, 15.
- Metcalf, T. R., Alexander, D.: 1999, *Astrophys. J.* **522**, 1108.
- Metcalf, T. R., Alexander, D., Hudson, H. S., Longcope, D. W.: 2003, *Astrophys. J.* **595**, 483.
- Nakajima, H., Sekiguchi, H., Sawa, M., Kai, K., Kawashima, S.: 1985, *Publ. Astron. Soc. Japan* **37**, 163.
- Nakajima, H., Nishio, M., Enome, S., Shibasaki, K., Takano, T., Hanaoka, Y., *et al.*: 1994, *Proc. IEEE* **82**, 705.
- Preka-Papadema, P., Alissandrakis, C. E.: 1992, *Astron. Astrophys.* **257**, 307.
- Qiu, J., Lee, J., Gary, D. E., Wang, H.: 2002, *Astrophys. J.* **565**, 1335.
- Ramaty, R.: 1969, *Astrophys. J.* **158**, 753.
- Ramaty, R., Schwartz, R. A., Enome, S., Nakajima, H.: 1994, *Astrophys. J.* **436**, 941.
- Scherrer, P. H., Bogart, R. S., Bush, R. I., Hoeksema, J. T., Kosovichev, A. G., Schou, J., *et al.*: 1995, *Solar Phys.* **162**, 129.
- Silva, A. V. R., Wang, H., Gary, D. E.: 2000, *Astrophys. J.* **545**, 1116.
- Takasaki, H., Kiyohara, J., Asai, A., Nakajima, H., Yokoyama, T., Masuda, S., Sato, J., Kosugi, T.: 2007, *Astrophys. J.* **661**, 1234.
- Torii, C., Tsukiji, Y., Kobayashi, S., Yoshimi, N., Tanaka, H., Enome, S.: 1979, *Proc. Res. Inst. Atmospheric* **26**, 129.
- White, S. M., Krucker, S., Shibasaki, K., Yokoyama, T., Shimojo, M., Kundu, M. R.: 2003, *Astrophys. J. Lett.* **595**, 111.
- White, S. M., Thomas, R. J., Schwartz, R. A.: 2005, *Solar Phys.* **227**, 231.
- Wild, J. P., Smerd, S. F., Weiss, A. A.: 1963, *Annu. Rev. Astron. Astrophys.* **1**, 291.

